This is a preprint, the final version is subject to change, of the American Mineralogist (MSA)
Cite as Authors (Year) Title. American Mineralogist, in press.
DOI: https://doi.org/10.2138/am-2019-6807

Revision 1

Evidence for syngenetic micro-inclusions of As^{3+}- and As^{5+}-containing Cu sulfides in hydrothermal pyrite

Margarita Merkulova*[1], Magdalena Murdzek[1], Olivier Mathon[1], Pieter Glatzel[1], Valentina Batanova[2], Alain Manceau[2]

[1]European Synchrotron Radiation Facility (ESRF), 71 Rue des Martyrs, 38000 Grenoble, France
[2]Univ Grenoble Alpes, CNRS, ISTerre, CS 40700, 38058 Grenoble, France

*margarita.merkulova@esrf.fr

Most frequently arsenic is nominally monovalent (As^{1-}) in pyrite (FeS_2) and substituted for S. Nominally trivalent arsenic (As^{3+}) has been reported previously in hydrothermal Peruvian pyrite and was considered to be substituted for Fe based on the negative correlation between the concentrations of the two elements. Here, we provide the first observation of the incorporation of As^{3+} in goldfieldite ($Cu_{12}(As,Sb,Bi)_2Te_2S_{13}$) and As^{5+} in colusite ($Cu_{26}V_2(As,Sb)_4Sn_2S_{32}$) inclusions in As^{1-}-pyrite from high-sulfidation deposits in Peru. This information was obtained by combining spatially-resolved electron probe (EPMA), synchrotron-based X-ray fluorescence (SXRF) and absorption spectroscopy (micro-XANES and micro-EXAFS) with new high energy-resolution XANES spectroscopy (HR-XANES). The two Cu sulfide inclusions range from several to one hundred micrometers in size and the As^{3+}/As^{5+} concentration varies from a few parts-per-million (ppm) to a maximum of 17.33 wt%, compared to a maximum of 50 ppm As^{1-} in pyrite. They also contain variable amounts of Sn (18.47 wt% max.), Te (15.91 wt% max.), Sb (8.54 wt% max.), Bi (5.53 wt% max.), and V (3.25 wt% max.). The occurrence of As^{3+}/As^{5+}-containing sulfosalts in As^{1-}-containing pyrite grains indicates that oxidizing hydrothermal conditions prevailed during the late stage of the mineralization process in the ore deposits from Peru.

Keywords: Pyrite, goldfieldite, colusite, arsenic, high-sulfidation deposits

Introduction

In sulfide ore deposits, arsenic occurs commonly as realgar (As_4S_4), orpiment (As_2S_3), and arsenopyrite (FeAsS), and less commonly as enargite (Cu_3AsS_4), tennantite ($Cu_{12}As_4S_{13}$), and luzonite (Cu_3AsS_4) (Fleet and Mumin 1997; Baumgartner et al. 2008; Bendezu and Fontboté 2009). Even more frequently, however, As occupies substitutional position, as in pyrite (FeS_2) and in complex sulfosalt minerals, such as colusite (Spry et al. 1994). Arsenian pyrite is of particular interest because it can contain as much as ~20 wt% As in hydrothermal Au deposits (Reich et al. 2005), and the release of As in acid mine drainage poses a threat to ecosystems and humans.

Arsenic is nominally trivalent (As^{3+}) in tennantite (Moelo et al. 2008) and five-valent (As^{5+}) in enargite (Kouzmanov et al. 2004), colusite (Frank-Kamenitskaya et al. 2002), and luzonite (Moelo et al. 2008). It can occur in three oxidation states in arsenian pyrite. The usual type is As^{1-}. As^{1-}-pyrite is abundant in Carlin-type and low-sulfidation epithermal and hydrothermal gold deposits (e.g., Simon et al. 1999; Savage et al. 2000; Paktunc 2008; Deditius et al. 2014). The nominal 1- oxidation state was informed by XANES spectroscopy (e.g., Simon et al. 1999; Paktunc 2008), and on the basis of EXAFS spectroscopy As substitutes for S (Savage et al. 2000). Indirect structural evidence for this substitution is provided by the negative correlation between S and As concentrations (Fleet et al. 1989; Deditius et al. 2014).

A second type, As^{3+}-pyrite, has been described in high-sulfidation epithermal deposits from Peru and Japan and is considered to be formed under oxidizing conditions (Deditius et al. 2008; Tanimizu et al. 2009). The 3+ oxidation state was established by XPS and XANES, and Deditius et al. (2008) suggested that As^{3+} substitutes for Fe based on the negative

53 correlation between the two elements measured by EPMA. Chouinard et al. (2005) had
54 suggested earlier that one As^{3+} and one Ag^{+} substitute for two Fe^{2+}, effectively balancing the
55 total charge.

56 A third type, As^{2+}-pyrite, has been reported from hydrothermal synthesis with As_2O_3
57 and $Na_2HAsO_4 \bullet 7H_2O$ (Qian et al. 2013). A nominal oxidation state of 2+ was derived from
58 the comparison with the XANES spectrum of realgar ($As^{2+}_4S_4$) and by XPS. Incorporation of
59 $As^{2+/3+}$ at the Fe site in synthetic pyrite has been demonstrated by EXAFS supplemented with
60 density functional theory (DFT) (Le Pape et al. 2017). Despite these progresses in the
61 identification and characterization of the oxidized forms of As in pyrite, their structural
62 chemistry is as yet unknown in natural pyrite. There is no firm indication that As^{3+} substitutes
63 for Fe^{2+}, nor that As^{2+} naturally exists in pyrite, and arsenian pyrite can contain micro-
64 inclusions of As^{3+}/As^{5+} Cu sulfides (Huston et al. 1995; Vikentyev et al. 2004; Pačevsky et al.
65 2008).

66 In this study, we used high energy-resolution XANES (HR-XANES) and laterally-
67 resolved micro-XANES and micro-EXAFS spectroscopy, in combination with synchrotron-
68 based X-ray fluorescence (SXRF) elemental mapping and electron probe microanalysis
69 (EPMA), to determine the oxidation state and crystal chemistry of As in three hydrothermal
70 pyrite from Peru. As^{3+} and As^{5+} were identified in Cu-sulfide minerals that represent
71 inclusions in the three pyrite. This work is the first to show As K-edge XANES and EXAFS
72 measurements on Cu-sulfide minerals, here goldfieldite and colusite, and to report their
73 structural formulae. The results provide new insights into the substitutional mechanisms of
74 As^{3+} and As^{5+} in copper sulfosalts that are common in polymetallic epithermal deposits.
75

76 **Materials and methods**

One pyrite comes from the Huanzala mine in central Peru (2P), another from the Canchaque mining district in northern Peru (3P), and the third is from an unknown Peruvian locality (1P). The three specimen are massive aggregates of pyrite crystals up to 8 mm in size (Supplementary Fig. S1). Parts of the samples were ground into powder in a glove bag filled with He to prevent oxidation. Mineralogical purity was verified by X-ray diffraction (Supplementary Fig. S2) and chemical composition was analyzed by inductively coupled plasma-mass spectrometry (ICP-MS). Powder HR-XANES measurements were performed on beamline ID26 at the European Synchrotron Radiation Facility (ESRF, Grenoble) using a high-luminosity crystal multianalyzer (Rovezzi et al., 2017). This analyzer provides the resolution that is needed to remove the intense background signal coming from the Fe $K_{\alpha/\beta}$ fluorescence and the Compton and elastic scattering, which otherwise would saturate the detector in total fluorescence yield (TFY) detection mode (Supplementary material). Fragments of pyrite crystals were embedded in epoxy resin and polished for EPMA, SXRF mapping, micro-XANES and micro-EXAFS in TFY. X-ray micro analysis and spectroscopy were performed on the ESRF beamline BM23. The reference compounds used for HR-XANES and TFY-XANES spectroscopy (FeAsS, As_4S_4, As_2O_3, As_2O_5) were diluted in NB to prevent overabsorption (Manceau et al. 2002). Only the energy of the white line, which is independent of the mode of measurement, is used in the comparison of HR-XANES and TFY-XANES spectra. The methods are detailed in the Supplementary material.

Results and discussion

Element composition and distribution

Trace element contents vary by a factor of approximately two in the three bulk pyrite (Table 1). As concentrations range from 122 ppm to 265 ppm, Cu concentrations from 1376 ppm to 2838 ppm, Sb concentrations from 42 ppm to 76 ppm, and Bi concentrations from 126

ppm to 164 ppm. Microscopic observations and analyses show that these elements are not uniformly distributed within each pyrite grain. No growth-zoning compositional variations are observed on bulk BSE images (Fig. 1). However, <1 – 200 μm inclusions of brighter BSE intensity, thus from higher Z elements than Fe in pyrite, are observed in all grains. Some of the inclusions are concentrically aligned, probably perpendicularly to the growth direction (Brooker et al. 1987). Outer parts of pyrite grains usually lack inclusions (Fig. 1 and Supplementary Fig. S3).

EPMA analyses of As and Cu in pyrite crystals range from the minimum detection limit of 20 ppm to a maximum of As = 50 ppm and Cu = 80 ppm. Zn, Te, Bi, V, and Sn are below the detection limits (b.d.l., Table S1). EPMA analyses of the pyrite inclusions show large mineralogical variability within the Cu-sulfide compositional fields of enargite (Cu_3AsS_4), Sn-rich colusite ($Cu_{26}V_2As_4Sn_2S_{32}$), the solid-solution between the end-members tennantite ($Cu_{12}As_4S_{13}$) and stoichiometric goldfieldite ($Cu_{10}Te_4S_{13}$, henceforth arsenian goldfieldite abbreviated as As- goldfieldite), bornite (Cu_5FeS_4), and a sulfide from the mawsonite group ($Cu_6Fe_2SnS_8$; Table S2). The five Cu-sulfides are present in pyrite 3P, four of them, enargite, colusite, goldfieldite, and mawsonite, are present in 1P, and only colusite and bornite are present in 2P (Fig. 1). As concentration varies from 16.77-17.33 wt% in enargite down to b.d.l.-2.96 wt% in bornite and mawsonite. Apart from As, the Cu-sulfides have elevated concentrations of Sb (up to 8.54 wt% in As-goldfieldite), Bi (up to 5.53 wt% in As-goldfieldite), V (up to 3.25 wt% in colusite), Sn (up to 18.47 wt% in mawsonite), and Te (8.37-15.91 wt%. in As-goldfieldite).

The high concentration of As and its detection in almost all point analyses allow estimating the weight proportion of the Cu-sulfide inclusions in the pyrite grains. Dividing the As bulk concentrations of 122 ppm in 1P, 265 ppm in 2P, and 169 ppm in 3P by the average As point concentrations of 7.46 wt% in 1P inclusions, 8.34 wt% in 2P inclusions, and 6.51

wt% in 3P inclusions yields 0.2% for 1P, 0.3% for 2P, and 0.3% for 3P. This proportion is remarkably constant. This finding can be rationalized genetically in terms of the contemporaneity of the circulating hydrothermal fluids at the origin of the Cu-sulfide precipitates in the three pyrite grains.

Colusite and As-goldfieldite are examined in more detail below for three reasons. First, they are by far the two most abundant Cu-sulfides in the pyrite grains. Out of 39 EPMA analyses, each Cu-sulfide mineral was identified 14 times (Table S2). Second, their composition is variable and nonstoichiometric as a result of homovalent and heterovalent coupled substitutions and the associated occurrence of vacancies. Third, arsenic is considered to be five-valent in colusite and trivalent in As-goldfieldite, yet its formal oxidation state has never been determined directly by X-ray absorption spectroscopy.

Chemical formulae

The nonstoichiometric formula of As-goldfieldite can be written $Cu^{+}_{10+x}(As,Sb,Bi)^{3+}_{x}Te^{4+}_{4-x}S_{13}$ and the nonstoichiometric formula of colusite can be written $Cu^{+}_{24+x}V^{5+}_{2}(As,Sb)^{5+}_{6-x}Sn^{4+}_{x}S_{32}$ with $0 \leq x \leq 2$ (Spry et al. 1994; Pohl et al. 1996; Trudu and Knittel 1998; Frank-Kamenetskaya et al. 2002; Wagner and Monecke 2005). Vacancies do not exceed two per formula unit (*pfa*). The two sulfides may contain in addition minor Fe^{2+} and Zn^{2+} usually assigned to the Cu^{+} position. The chemical formulae of the two Cu-sulfides, calculated on the basis of 13 S and 32 S *pfa* and averaged over all EPMA point analyses, are:

As-goldfieldite: $(Cu^{+}_{11.9}Fe^{2+}_{0.4})(As^{3+}_{1.4}Sb^{3+}_{0.5}Bi^{3+}_{0.2})Te^{4+}_{1.6}S_{13}$

Colusite: $(Cu^{+}_{25.3}Fe^{2+}_{0.7})(V^{5+}_{1.7}Fe^{2+}_{0.6})(As^{5+}_{3.3}Sb^{5+}_{0.3})Sn^{4+}_{2.0}S_{32}$

The colusite chemical formulae are close to the ideal stoichiometry of $Cu_{26}V_2As_4Sn_2S_{32}$ in 2P only. The total number of cations in the average formulae is 16.18 for As-goldfieldite and 33.83 for colusite, close to the number of crystallographic sites *pfa* of 16 and 34, respectively. Therefore, the two minerals have few vacancies. The total cationic charges are 25.88 for As-

goldfieldite and 62.11 for colusite, in good compliance with the formula unit for As-goldfieldite (2 x 13 = 26), but in a deficit of (2 x 32.0) - 61.1 = 2.9 positive charges for colusite. The charge unbalance in 1P and 3P arises from a deficiency in As^{5+} and V^{5+} and could be compensated by assuming that Fe is partly trivalent in the structure, for instance at the V^{5+} interstitial site (Kouzmanov et al., 2004). Filling up this site with Fe in the average formula is supported by the Pearson analysis, which shows a statistically significant negative correlation between Fe and V ($r = -0.98$ at $P = 0.05$).

Oxidation state of As in bulk pyrite grains

Pyrite 1P, 2P, and 3P have nearly identical HR-XANES shape and a white line energy position intermediate between those of arsenopyrite ($FeAs^{1-}S$, 11867.6 eV) and $As^{3+}_2O_3$ (11870.0 eV; Figs. 2a and 2b). From the first derivative, the XANES maxima are at 11869.4 eV for 3P and 11869.7 eV for 1P and 2P. With a precision on the energy measurement of 0.1 eV (see SI), the chemical shift of 0.3 eV between $As^{3+}_2O_3$ and 1P/2P on the one hand, and between 1P/2P and 3P on the other hand, is significant. It suggests a valence mixture of As in the three samples and a higher proportion of reduced As in 3P. Distinction of 3P from 1P and 2P is also apparent in the low-energy absorption tail at 11864.0-11866.0 eV (arrow in Fig. 2a).

Oxidation state of As in pyrite and in Cu-sulfide inclusions

Five micro-XANES spectra were measured on points of interest from the SXRF map of 3P (Fig. 3). One spectrum was taken in pyrite (spot 1) and two spectra on As-goldfieldite (spots 2 and 3) and two on colusite (spots 4 and 5). The pyrite spectrum is at the white line energy of arsenopyrite ($FeAs^{1-}S$), as is known when As^{1-} substitutes for S^{1-} in the pyrite structure (Simon et al. 1999; Paktunc 2008). Less directly evident, the colusite spectrum is at the energy of $As^{3+}_2O_3$ (11870.0 eV). The same energy match with $As^{3+}_2O_3$ was observed previously for enargite (Cu_3AsS_4; Di Benedetto et al. 2011). Since As is +5 in the two sulfides

(Pauporté and Lincot 1995; Frank-Kamenitskaya et al. 2002), we come to the definite conclusion that the absorption energy of $As^{3+}_2O_3$ is characteristic of As^{5+} in sulfide minerals. The leftward shift of 3.5 eV between As^{5+}-colusite/enargite and $As^{5+}_2O_5$ (11873.5 eV) results from the higher covalent character of the As-S bond than the As-O bond. Dependence of the absorption edge energy on the metal-ligand bonding has been observed previously for As^{3+}/As^{5+} and Cu^{+}/Cu^{2+} coordination complexes with O and S donors (Kau et al. 1987; Smith et al. 2005), and for Cu^{+}/Cu^{2+} oxides and sulfides (Manceau and Matynia 2010). The absorption edge of As-goldfieldite is at 11868.5 eV, between those of As^{1-}-pyrite and As^{5+}-colusite. This white line energy position is assigned to As^{3+} on the basis of the known crystal chemistry of goldfieldite (Pohl et al. 1996; Trudu and Knittel 1998; Di Benedetto et al., 2011).

The proportions of the oxidized (As^{5+}) and reduced (As^{1-} + As^{3+}) forms of arsenic in the pyrite grains can be estimated from the absorption energy of the bulk spectra. Bulk XANES is a weighted sum of all As species in the pyrite grains that include As^{1-}-pyrite, As^{3+}-goldfieldite, and As^{5+}-containing Cu-sulfides (colusite, enargite, and likely mawsonite). The fractional amount of each oxidation state cannot be estimated univocally from the white line energy position of bulk XANES because there are three unknowns instead of two maxima for a regression analysis of the white line energy. For instance, a bulk average energy of 11868.5 eV may correspond to 100% As^{3+}-goldfieldite or to 60% As^{1-}-pyrite + 40% As^{5+}-colusite/enargite (11867.6 x 0.6 + 11870.0 x 0.4 = 11868.5). The white line energy of 1P/2P (11869.7 eV) can be obtained with 10% As^{1-} + 90% As^{5+} and with 20% As^{3+} + 80% As^{5+}, and the white line energy of 3P with 25% As^{1-} + 75% As^{5+} and with 40% As^{3+} + 60% As^{5+}. Grouping together the two indistinguishable reduced forms, one gets 15% As^{1-}/As^{3+} + 85% As^{5+} for 1P/2P and 30% As^{1-}/As^{3+} + 70% As^{5+} for 3P. Thus, mainly As^{5+} is detected by bulk XANES, which is consistent with the abundance of As^{5+}-containing colusite and occurrence

of As^{5+}-rich enargite in the Cu-sulfide inclusions (Table S2). Although As^{1-} probably occurs throughout the pyrite crystals, here it is a minor species while in other geological settings it is dominant (Savage et al. 2000).

Coordination of As in Cu-sulfide inclusions

As K-edge micro-EXAFS spectra were measured on As-goldfieldite (spot 2) and colusite (spot 4). The spectrum of colusite was fit with 4 S atoms at 2.23 Å, 6.8 Cu atoms at 3.64 Å and 5.2 Cu atoms at 3.81 Å (Fig. 4a and Supplementary Table S3) The EXAFS parameters agree with the sphalerite-type structure of colusite and with the d(As-S) = 2.20 Å and d(As-Cu) = 3.66-3.73 Å distances determined by single-crystal structural refinement (Spry et al. 1994). The twelve As-Cu pairs across the tetrahedral corner linkages are at the same distance in sphalerite (space group *F*-43*m*), whereas they are split in colusite (space group *P*-43*n*). The higher structural disorder of colusite was confirmed by fitting its EXAFS spectrum with one Cu shell instead of two in the best-fit calculation (Fig. 4b). This model-fit does not replicate well all the EXAFS structures and yields 2.5 Cu neighbors instead of 12 and an unrealistically low Debye-Waller factor (σ = 0.005 Å). The local structure of the As environment is even more disordered in As-goldfieldite since only the first S shell is detected in this mineral. Best fit results are obtained with 3 S atoms at 2.27 Å (Fig. 4c), in agreement with the As^{3+} for Te^{4+} substitution at the three-fold pyramidal site determined by Rietveld refinement (Pohl et al. 1996). The crystallographic As^{3+}-S distance is however unknown because As has a site occupancy of 0.1 in the refined structure. The average d($Te_{0.625}Sb_{0.25}As_{0.125}$)-S crystallographic value is 2.31 Å. The shorter As-S bond length observed here is consistent with the smaller ionic radius of As^{3+} than Te^{4+}.

Implications

The association of pyrite with Cu-bearing minerals, such as enargite, colusite, As-goldfieldite and mawsonite, is common in high-sulfidation deposits (e.g., Mancano and Campbell 1995; Baumgartner et al. 2008; Bendezu and Fontboté 2009; Franchini et al. 2015), and has been described previously in the porphyry Cu-Au deposit from Peru (Baumgartner et al. 2008; Bendezu and Fontboté 2009; Catchpole et al. 2012; Fontboté et al., 2017). However, to our knowledge occurrences of As-goldfieldite and colusite in Canchaque mine (Carlson and Sawkins 1980) and As-goldfieldite in Huanzala mine (Imai et al. 1985; Imai 1999) in Peru have never been described before. From a genetic perspective, the distribution, composition, and crystal chemistry of the sulfosalt inclusions help unravel the ore formation in Peruvian deposits.

The crudely concentric patterns of the inclusions that probably parallel the radial growth of the pyrite crystals, and the relatively large crystal sizes (up to 100 μm), suggest that the inclusions are syngenetic (Craig et al. 1998). The Cu-sulfide minerals and the host pyrite belong to the main ore stage formation that followed the early quartz-pyrite stage (e.g., Carlson and Sawkins 1980; Imai et al. 1985; Bendezu and Fontboté 2009). Formation of pyrite is typical in the main ore-forming stage in Peruvian deposits including Huanzala mine (Imai et al. 1985). The presence of colusite, enargite, As-goldfieldite and mawsonite indicate high-sulfidation conditions and low to medium temperatures (~200-300ºC) of the hydrothermal fluid during the main ore-forming stage (Bendezu and Fontboté 2009; Dill et al. 2010; Catchpole et al. 2012). Moreover, the high valence states of As in Cu-sulfides suggest that the ore-forming fluid had high f_{O2} (Kase et al. 1994; Trudu and Knittel 1998). The absence of the Cu-sulfide mineral inclusions in the outer parts of pyrite grains suggests that the circulating hydrothermal fluid was depleted in Cu, As, Te, Sb, Sn, V and Bi, and designates the termination of the ore-forming process. Thus, detailed investigation of pyrite provides insight into the evolution of the hydrothermal process.

Hot spots of arsenic in pyrite inclusions may cause confusion in identifying its speciation when the host crystal contains As^{3+} in its structure. This situation can be encountered in high-sulfidation epithermal deposits, such as occurs in the Yanacocha gold setting from northwest of Peru. This deposit contains trivalent arsenic in the form of As^{3+}-pyrite, in which As^{3+} substitutes for Fe (Deditius et al. 2008). However, other minerals containing oxidized forms of arsenic, including enargite and tennantite, have been reported in this mineralized setting (Longo et al. 2010; Teal and Benavides 2010). Thus, if caution is not exercised, there can be an ambiguity on the chemical and structural form of As. In general a combination of bulk averaging and laterally-resolved analytical and spectroscopic techniques is ideally suited for evaluating trace element distributions and chemical speciation in pyrite, especially of hydrothermal origin.

From an environmental perspective, high concentrations of potentially toxic As, Cu, Te, Sn, Sb, and Bi in pyrite, which at first sight appears pure when massive and shiny like here (Fig. S1), may pose a specific threat to ecosystems in acid mine drainage settings. Even more toxic and little studied is thallium, which is classified as a priority contaminant by the U.S. Environmental Protection Agency. Its speciation in geogenic pyrite is as yet unknown (D'Orazio et al. 2017), and the combination of techniques used in this study offers a unique access to the problem.

References

Baumgartner, R., Fontboté, L., and Vennemann, T. (2008) Mineral zoning and geochemistry of epithermal polymetallic Zn-Pb-Ag-Cu-Bi mineralization at Cerro de Pasco, Peru. Economic Geology, 103(3), 493–537.

Bendezú, R., and Fontboté, L. (2009) Cordilleran epithermal Cu-Zn-Pb-(Au-Ag) mineralization in the Colquijirca district, central Peru: Deposit-scale minera logical patterns. Economic Geology, 104(7), 905–944.

Brooker, D.D., Craig, J.R., and Rimstidt, J.D. (1987) Ore metamorphism and pyrite porphyroblast development at the Cherokee mine, Ducktown, Tenessee. Economic Geology, 82, 72-86.

Carlson, S., and Sawkins, F.J. (1980) Mineralogic and fluid inclusion studies of the Turmalina Cu-Mo-bearing breccia pipe, Nothern Peru. Economic Geology, 75(8), 1233–1238.

Catchpole, H., Kouzmanov, K., and Fontboté, L. (2012) Copper-excess stannoidite and tennantite-tetrahedrite as proxies for hydrothermal fluid evolution in a zoned cordilleran base metal district, Morococha, Central Peru. Canadian Mineralogist, 50(3), 719–743.

Chouinard, A., Paquette, J., and Williams-Jones, A.E. (2005) Crystallographic controls on trace-element incorporation in Auriferous pyrite from the Pascua epithermal high-sulfidation deposit, Chile-Argentina. Canadian Mineralogist, 43(3), 951–963.

Craig, J.R., Vokes, F.M., and Solberg, T.N. (1998) Pyrite: physical and chemical textures. Mineralium Deposita, 34(1), 82–101.

D'Orasio, M., Biagioni, C., Dini, A., Vezzoni, S. (2017) Thallium-rich pyrite ores from the Apuan Alps, Tuscany, Italy: constraints for their origin and environmental concerns. Mineralium Deposita, 52(5), 687-707.

Deditius, A.P., Reich, M., Kesler, S.E., Utsunomiya, S., Chryssoulis, S.L., Walshe, J., and Ewing, R.C. (2014) The coupled geochemistry of Au and As in pyrite from hydrothermal ore deposits. Geochimica et Cosmochimica Acta, 140, 644–670.

Deditius, A.P., Utsunomiya, S., Renock, D., Ewing, R.C., Ramana, C.V., Becker, U., and Kesler, S.E. (2008) A proposed new type of arsenian pyrite: Composition,

299 nanostructure and geological significance. Geochimica et Cosmochimica Acta, 72(12),
300 2919–2933.
301 Di Benedetto, F., Pelo, S. Da, Caneschi, A., and Lattanzi, P. (2011) Chemical state of arsenic
302 and copper in enargite : evidences from EPR and X-ray absorption spectroscopies and
303 SQUID magnetometry. Neues Jahrbuch für Mineralogie – Abhandlungen, 188/1, 11–
304 19.
305 Dill, H.G. (2010) The "chessboard" classification scheme of mineral deposits: Mineralogy
306 and geology from aluminum to zirconium. Earth-Science Reviews. 100(1–4), 1–420.
307 Fleet, M.E., MacLean, P.J., and Barbier, J. (1989) Oscillatory-zoned As-bearing pyrite from
308 strata-bound and stratiform gold deposits; an indicator of ore fluid evolution.
309 Economic Geology Monograph. 6, 356-362.
310 Fleet, M.E., and Mumin, A.H. (1997) Gold-bearing arsenian pyrite and marcasite and
311 arsenopyrite from Carlin Trend gold deposits and laboratory synthesis. American
312 Mineralogist. 82, 182-193.
313 Fontboté, L., Kouzmanov, K., Chiaradia, M., and Pokrovski, G.S. (2017) Sulfide minerals in
314 hydrothermal deposits. Elements, 13, 97-103.
315 Franchini, M., McFarlane, C., Maydagán, L., Reich, M., Lentz, D.R., Meinert, L., and
316 Bouhier, V. (2015) Trace metals in pyrite and marcasite from the Agua Rica
317 porphyry-high sulfidation epithermal deposit, Catamarca, Argentina: Textural features
318 and metal zoning at the porphyry to epithermal transition. Ore Geology Reviews. 66,
319 366–387.
320 Frank-Kamenetskaya, O.V., Rozhdestvenskaya, I.V., and Yanulova, L.A. (2002) New data on
321 the crystal structures of colusite and arsenosulvanites. Journal of Structural Chemistry,
322 43(1), 89–100.

Huston, D.L., Sie, S.H., Suter, G.F., Cooke, D.R., and Both, R.A. (1995) Trace elements in sulfide minerals from eastern Australian volcanic- hosted massive sulfide deposits: part I. Proton microprobe analyses of pyrite, chalcopyrite, and sphalerite, and part II. Selenium levels in pyrite: comparison with $\delta^{34}S$ values and implications for the source of sulfur in volcanogenic hydrothermal systems. Economic Geology. 90(5), 1167–1196.

Imai, H., Kawasaki, M., Yamaguchi, M., and Takahashi, M. (1985) Mineralization and paragenesis of the Huanzala mine, central Peru. Economic Geology. 80(2), 461–478.

Imai, H. (1999) Mineralizations of base metal deposits of acid-sulfate type coexisting with Adularia-Sericite type. Resource Geology. 49(3), 147-156.

Kase, K., Yamamoto, M., Mitsuno, C. (1994) Germanium-bearing colusite from the Yanahara mine, Japan, and its significance to ore genesis. Resource Geology, 44(1), 33-38.

Kau, L-S., Spira-Solomon, D.J., Penner-Hahn, J.E., Hodgson, K.O., Solomon, E.I. (1987) X-ray absorption edge determination of the oxidation state and coordination number of copper: application to the type 3 site in Rhus vernicifera laccase and its reaction with oxygen. Journal of the American Chemical Society, 109, 6433-6442.

Kouzmanov, K., Ramboz, C., Bailly, L., and Bogdanov, K. (2004) Genesis of high-sulfidation vinciennite-bearing Cu-As-Sn (±Au) assemblage from the Radka epithermal copper deposit, Bulgaria: Evidence from mineralogy and infrared microthermometry of enargite. Canadian Mineralogist, 42(5), 1501–1521.

Le Pape, P., Blanchard, M., Brest, J., Boulliard, J., Ikogou, M., Stetten, L., Wang, S., Landrot, G., and Morin, G. (2017) Arsenic incorporation in pyrite at ambient temperature at both tetrahedral S^{-I} and octahedral Fe^{II} Sites: evidence from EXAFS−DFT analysis. Environmental Science and Technology. 51, 150-158.

Longo, A.A., Dilles, J.H., Grunder, A.L., and Duncan, R. (2010) Evolution of calc-alkaline volcanism and associated hydrothermal gold deposits at Yanacocha, Peru. Economic Geology. 105(7), 1191–1241.

Mancano, D.P., and Campbell, A.R. (1995) Microthermometry of enargite-hosted fluid inclusions from the Lepanto, Philippines, high-sulfidation CuAu deposit. Geochimica et Cosmochimica Acta, 59(19), 3909–3916.

Manceau, A., Marcus, M.A., and Tamura, N. (2002) Quantitative speciation of heavy metals in soils and sediments by synchrotron X‐ray techniques. In P.A. Fenter, M.L. Rivers, N.C. Sturchio and S.R. Sutton, Eds., Applications of Synchrotron Radiation in Low-Temperature Geochemistry and Environmental Science, 49, p. 341–428. Reviews in Mineralogy and Geochemistry, Mineralogical Society of America, Chantilly, Virginia.

Manceau, A., and Matynia, A. (2010) The nature of Cu bonding to natural organic matter. Geochimica et Cosmochimica Acta, 74, 2556-2580.

Moëlo, Y., Makovicky, E., Mozgova, N.N., Jambor, J.L., Cook, N., Pring, A., Paar, W., Nickel, E.H., Graeser, S., Karup-Møller, S., Balic-Žunic, T., Mumme, W.G., Vurro, F., Topa, D., Bindi, L., Bente, K., and Shimizu, M. (2008) Sulfosalt systematics: a review. Report of the sulfosalt sub-committee of the IMA Commission on Ore Mineralogy. European Journal of Mineralogy, 20(1), 7–46 .

Pačevski, A., Libowitzky, E., Živković, P., Dimitrijević, R., and Cvetković, L. (2008) Copper-bearing pyrite from the Čoka Marin polymetallic deposit, Serbia: Mineral inclusions or true solid-solution? Canadian Mineralogist, 46(1), 249–261.

Paktunc, D. (2008) Speciation of arsenic in pyrite by micro-X-ray absorption fine-structure spectroscopy (XAFS). ICAM Australia 2008, (September), 8–10.

Pauporté, T., and Lincot D. (1995) Electrical, optical and photo-electrochemical properties of natural enargite, Cu_3AsS_4. Advanced Materials for Optics and Electronics, 5, 289-298.

372 Pohl, D., Liessmann, W., and Okrugin, V.M. (1996) Rietveld analysis of selenium-bearing
373 goldfieldites. Neues Jahrbuch für Mineralogie – Monatshefte, 1-8.
374 Pokrovski, G.S., Borisova, A.Y., and Harrichoury, J.C. (2008) The effect of sulfur on vapor-
375 liquid fractionation of metals in hydrothermal systems. Earth and Planetary Science
376 Letters, 266, 345-362.
377 Pokrovski, G.S., Borisova, A.Y., and Bychkov, A.Y. (2013) Speciation and transport of
378 metals and metalloids in geological vapors. Reviews in Mineralogy and Geochemistry,
379 76 (1), 165-218.
380 Qian, G., Brugger, J., Testemale, D., Skinner, W., and Pring, A. (2013) Formation of As(II)-
381 pyrite during experimental replacement of magnetite under hydrothermal conditions.
382 Geochimica et Cosmochimica Acta, 100, 1–10.
383 Reich, M., Kesler, S.E., Utsunomiya, S., Palenik, C.S., Chryssoulis, S.L., and Ewing, R.C.
384 (2005) Solubility of gold in arsenian pyrite. Geochimica et Cosmochimica Acta,
385 69(11), 2781–2796.
386 Rovezzi M., Lapras, C., Manceau, A., Glatzel, P., and Verbeni, R. (2017) High energy-
387 resolution x-ray spectroscopy at ultra-high dilution with spherically bent crystal
388 analyzers of 0.5 m radius. Review of Scientific Instruments, 88(1), 013108.
389 Savage, K.S., Tingle, T.N., O'Day, P.A., Waychunas, G.A., and Bird, D.K. (2000) Arsenic
390 speciation in pyrite and secondary weathering phases, Mother Lode Gold District,
391 Tuolumne County, California. Applied Geochemistry. 15(8), 1219–1244.
392 Simon, G., Huang, H., Penner-Hahn, J.E., Kesler, S.E., and Kao, L.S. (1999) Oxidation state
393 of gold and arsenic in gold-bearing arsenian pyrite. American Mineralogist 84(7–8),
394 1071–1079.
395 Smith, P.G., Koch, I., Gordon, R.A., Mandoli, D.F., Chapman, B.D., and Reimer, K.J. (2005)
396 X-ray Absorption Near-Edge Structure Analysis of Arsenic Species for Application to

Biological Environmental Samples. Environmental Science and Technology, 39(1), 248–254.

Spry, P.G., Merlino, S., Wang, S., Zhang, X., and Buseck, P.R. (1994) New occurrences and refined crystal chemistry of colusite, with comparisons to arsenosulvanite. American Mineralogist, 79(7–8), 750–762.

Tanimizu, M., Takahashi, Y., Morishita, Y., and Shimada, N. (2009) Oxidation states of arsenic in pyrites. Photon Factory Activity Report 2008. 4, 2919–2919.

Teal, L., and Benavides, A. (2010) History and geologic overview of the Yanacocha mining district, Cajamarca, Peru. Economic Geology, 105(7), 1173–1190.

Testemale, D., Pokrovski, G.S., and Hazemann, J.L. (2011) Speciation of As^{III} and As^{V} in hydrothermal fluids by in situ X-ray absorption spectroscopy. European Journal of Mineralogy, 23, 379-390.

Trudu, A.G., and Knittel, U. (1998) Crystallography, mineral chemistry and chemical nomenclature of goldfieldite, the tellurian member of the tetrahedrite solid-solution series. Canadian Mineralogist, 36, 1115–1137.

Vikentev, I.V, Yudovskaya, M.A., Mokhov, A.V., Kerzin, A.L., and Tsepin, A.I. (2004) Gold and PGE in massive sulfide ore of the Uzelginsk deposit, Southern Urals, Russia. Canadian Mineralogist, 43, 651–665.

Wagner, T., and Monecke, T. (2005) Germanium-bearing colusite from the Waterloo volcanic-rock-hosted massive sulfide deposit, Australia: Crystal chemistry and formation of colusite-group minerals. Canadian Mineralogist, 43(2), 655–669.

Acknowledgments

The study was funded by ANR under Grant ANR-10-EQPX-27-01 (EcoX Equipex). We thank N. Findling for the XRD measurements and I. Sniguireva for help with the SEM measurements.

423

424 **Figure Legends**

425 **Figure 1.** Backscattered electron images of pyrite from Peru. The brighter zones are Cu
426 sulfides rich in As (up to 17.33 wt %), Sb, Sn, Te, and trace elements. The red rectangle
427 indicates the position of the SXRF map in Figure 3a.

428 **Figure 2.** (**a**) Bulk HR-XANES spectra from the three pyrite. Arrow indicates distinction of
429 3P from 1P and 2P in the low-energy absorption tail. (**b**) Bulk HR-XANES spectra of 1P
430 pyrite and As references: natural arsenopyrite (FeAsS) and realgar (As_4S_4), and synthetic
431 As_2O_3, and As_2O_5. Vertical lines indicate the white line energy positions for As^{1-} (11867.6
432 eV), As^{3+} in As_2O_3 (11870.0 eV) and As^{5+} in As_2O_5 (11873.5 eV).

433 **Figure 3.** (**a**) SXRF map of 3P pyrite. Map size: 240x280 μm^2, pixel size: 10x10 μm^2. (**b**)
434 micro TFY-XANES (pyrite, As-goldfieldite, colusite) and bulk HR-XANES spectra (As_2O_3,
435 As_2O_5). TFY-XANES spectra have a low-energy tail, which HR-XANES spectra do not have
436 because they were measured with a high energy-resolution crystal multianalyzer. However,
437 the energy of the white line is independent of the mode of measurements.

438 **Figure 4.** Micro-EXAFS spectra (**a, b, c**) and Fourier transforms (**d, e, f**) for colusite (spot 4
439 in Figure 3a) and As-goldfieldite (spot 2 in Figure 3a) with fits. The peak at about 2.5 Å on
440 the Fourier transform of colusite is unexplained. The analyzed colusite grain is from a single
441 crystal (Supplementary Fig. S10) and colusite does not have atomic pairs at this distance.

442

This is a preprint, the final version is subject to change, of the American Mineralogist (MSA)
Cite as Authors (Year) Title. American Mineralogist, in press.
DOI: https://doi.org/10.2138/am-2019-6807

Table 1. ICP-MS bulk analyses of trace elements in Peruvian pyrite

	Cr	Mn	Co	Ni	Cu	Zn	As	Se	Ag	Sb	W	Au	Hg	Pb	Bi
D.L.	0.5	5	0.5	0.5	0.5	5	5	2	0.5	0.5	0.5	2	0.05	0.5	0.5
1P Peru	6.4	150	4.7	3.9	1375.8	9	122	22	4.5	41.9	1.3	89	0.42	3	129.7
2P Peru	6.2	93	14.2	10.4	2498.8	27	265	49	9.4	16.1	1296.5	24	b.d.l.	123.3	164.5
3P Peru	b.d.l.	73	6	4.3	2837.9	19	169	21	11.1	76.2	5.2	150.5	0.37	4.8	126.3

Notes: All values are in ppm, except Au (ppb). Standard deviation (1σ) is ≤ 6.5% for all elements.
D.L. – detection limit; b.d.l. – below detection limit.
The high W content in 2P is attributed to sparse inclusions of scheelite ($CaWO_4$).

Figure 1

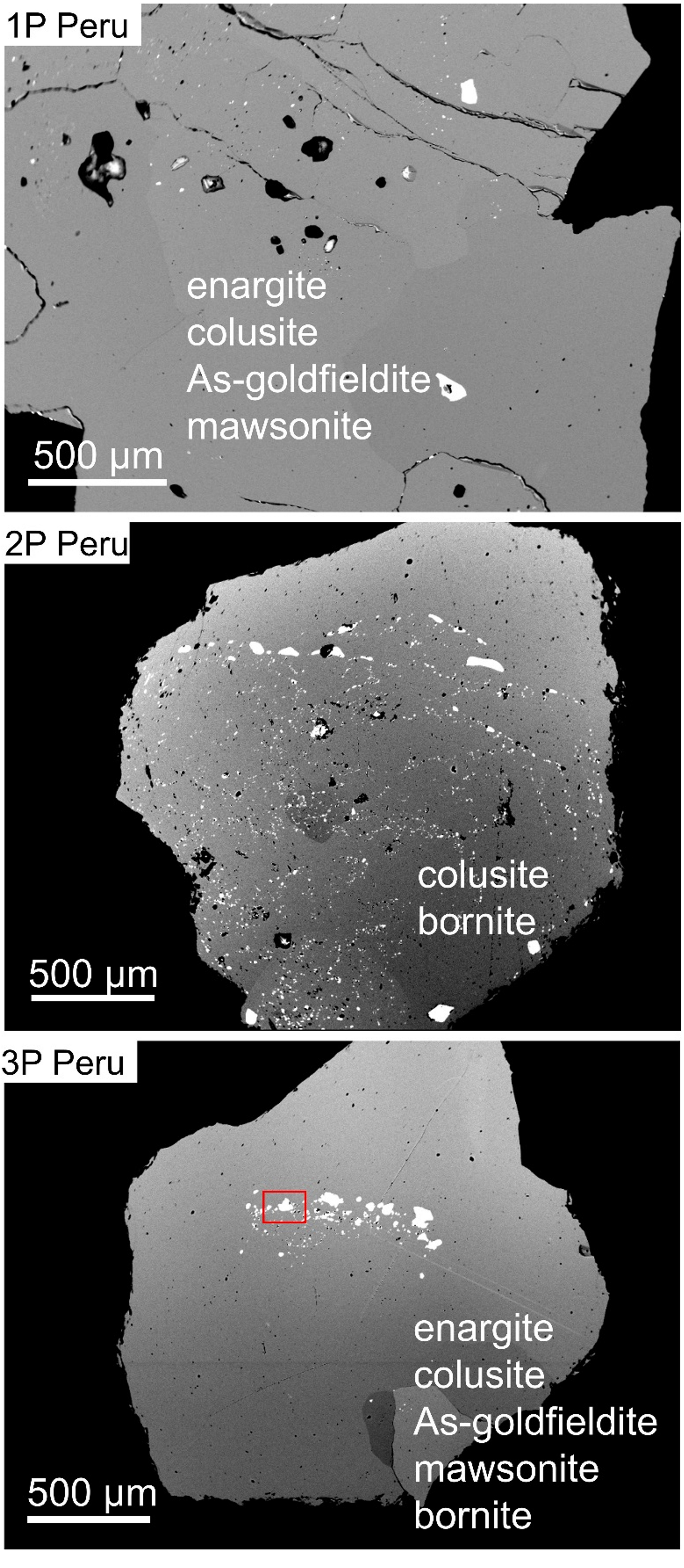

This is a preprint, the final version is subject to change, of the American Mineralogist (MSA)
Cite as Authors (Year) Title. American Mineralogist, in press.
DOI: https://doi.org/10.2138/am-2019-6807

Figure 2

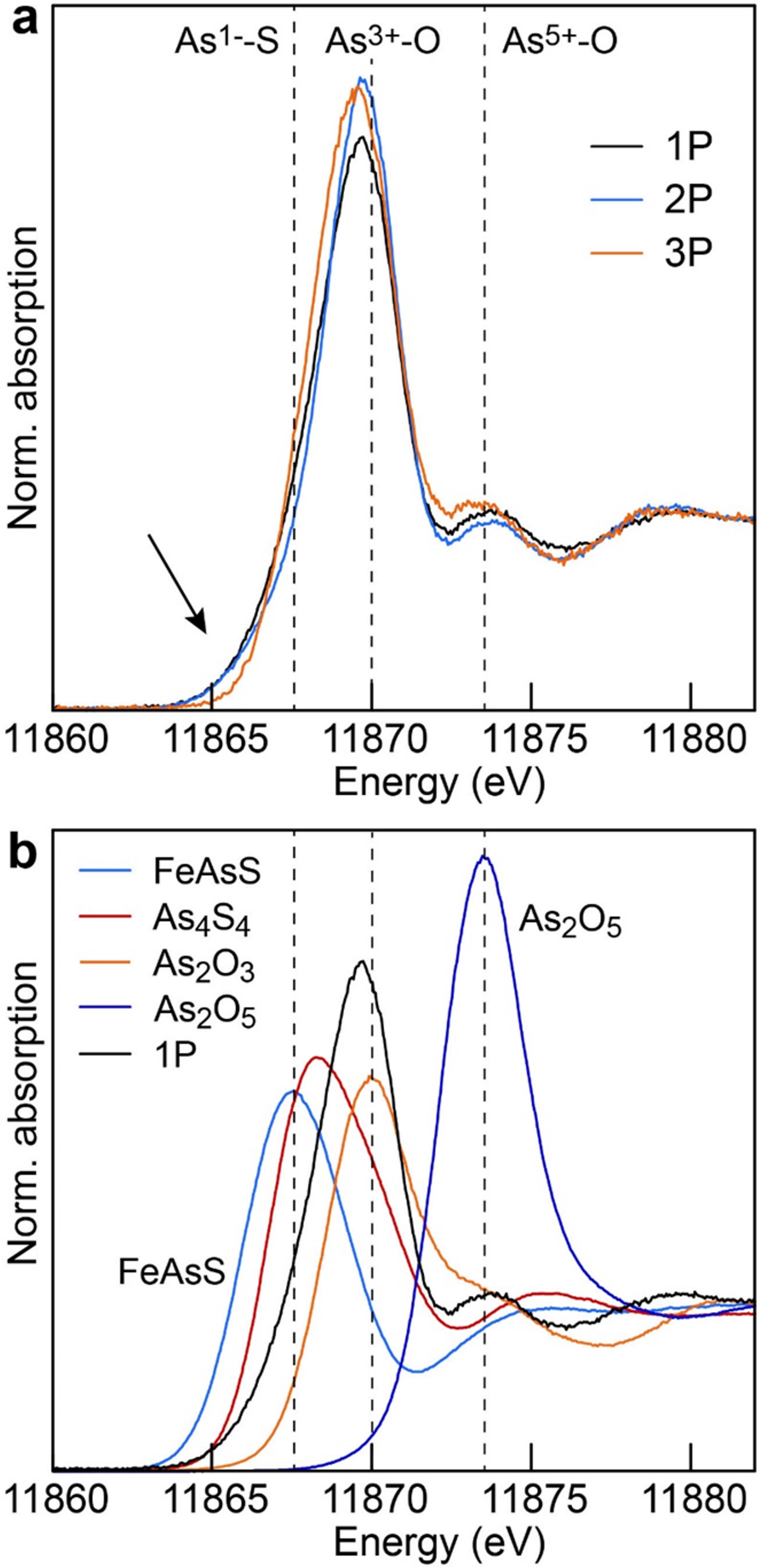

Figure 3

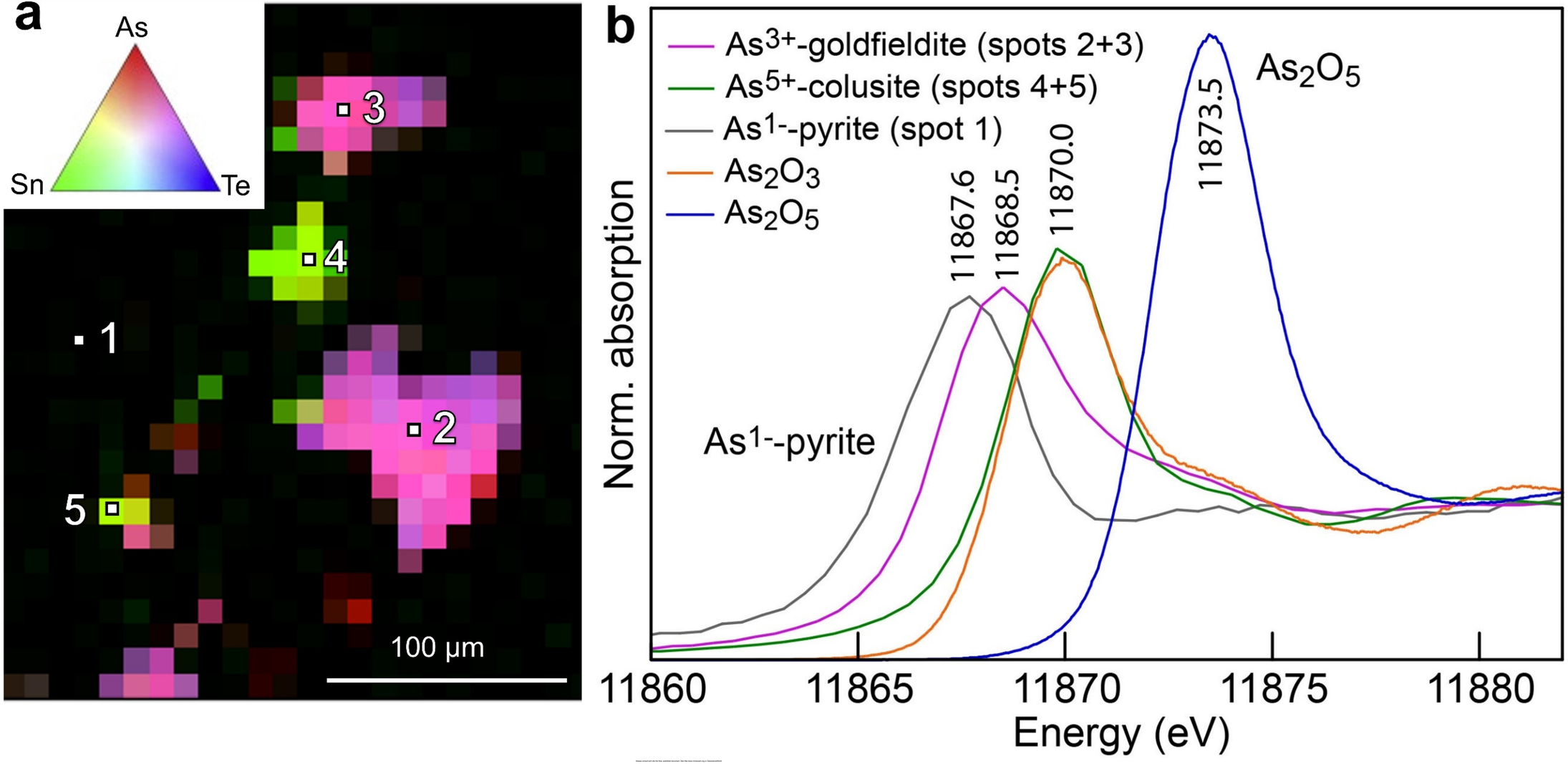
a
As
Sn
Te
1
2
3
4
5
100 µm
b
As3+-goldfieldite (spots 2+3)
As5+-colusite (spots 4+5)
As1--pyrite (spot 1)
As2O3
As2O5
11867.6
11868.5
11870.0
11873.5
As2O5
As1--pyrite
Norm. absorption
11860
11865
11870
11875
11880
Energy (eV)

Figure 4

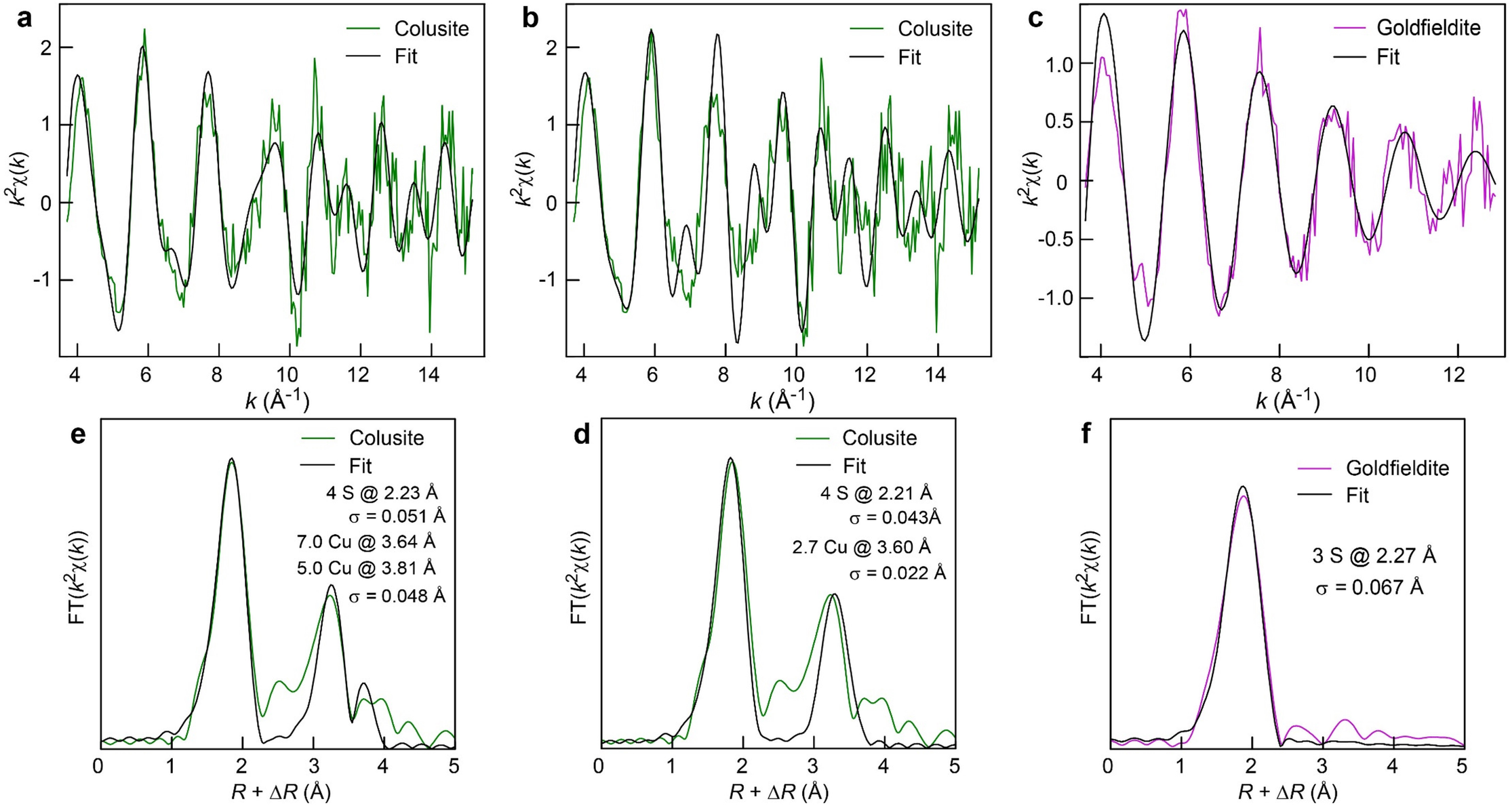
a
Colusite
Fit
$k^2\chi(k)$
k (Å^{-1})
b
Colusite
Fit
$k^2\chi(k)$
k (Å^{-1})
c
Goldfieldite
Fit
$k^2\chi(k)$
k (Å^{-1})
e
Colusite
Fit
4 S @ 2.23 Å
σ = 0.051 Å
7.0 Cu @ 3.64 Å
5.0 Cu @ 3.81 Å
σ = 0.048 Å
FT($k^2\chi(k)$)
$R + \Delta R$ (Å)
d
Colusite
Fit
4 S @ 2.21 Å
σ = 0.043Å
2.7 Cu @ 3.60 Å
σ = 0.022 Å
FT($k^2\chi(k)$)
$R + \Delta R$ (Å)
f
Goldfieldite
Fit
3 S @ 2.27 Å
σ = 0.067 Å
FT($k^2\chi(k)$)
$R + \Delta R$ (Å)